Published in final edited form as:
Nature. 2017 June 28; 546(7660): 632–636. doi:10.1038/nature22987.

Making waves in a photoactive polymer film

Anne Helene Gelebart[1,2], **Dirk Jan Mulder**[1], **Mike Varga**[3], **Andrew Konya**[3], **Ghislaine Vantomme**[2], **E.W. Meijer**[2], **Robin L.B. Selinger**[3,*], and **Dirk J. Broer**[1,2,*]

[1)]Department of Chemical Engineering and Chemistry- Laboratory for Functional Organic Materials and Devices (SFD)- Eindhoven University of Technology, Eindhoven, The Netherlands [2)]Institute for Complex Molecular Systems (ICMS)- Eindhoven University of Technology, Eindhoven, The Netherlands [3)]Chemical Physics Interdisciplinary Program, Liquid Crystal Institute, Kent State University, Kent, OH, USA

Abstract

Oscillating materials1–4 that adapt their shape in response to an external stimulus are of interest for emerging applications in medicine and robotics. Liquid crystal networks have a prominent role in this area because they can be programmed to undergo stimulus-induced deformations in a variety of geometries, including in response to light5,6. In order to make these polymer networks photoresponsive, azobenzene molecules are often incorporated7–11. Most examples in the literature report on bending responses of these azobenzene modified films, where relaxation after photo-isomerization is rather slow. Modification of the core or addition of substituents to the azobenzene moiety can lead to drastic changes in photophysical and photochemical properties12–15 giving opportunity to circumvent the use of a complex set-up. Here we report on the incorporation of azo-derivatives with fast thermal relaxation into liquid crystal network films (LCN), to generate films that can exhibit continuous, directional macroscopic mechanical waves under constant light illumination, with a feedback loop driven by self-shadowing. A theoretical model and numerical simulation demonstrate this mechanism and show good qualitative agreement with experiments. We explore potential applications in light-driven locomotion and self-cleaning surfaces.

*Correspondence and requests for materials should be addressed to DJB for the experimental part D.Broer@tue.nl and to RLBS for the theoretical part rselinge@kent.edu.

Author contributions

AHG and DJM designed the experiments. AHG studied the macroscopic deformations and analyzed the results. DJM synthesized the compound I. GV synthesized the compound II. MV and AK developed the theoretical model. DJB supervised the overall research. EWM participated in the interpretation of the results. RLBS supervised the theoretical modeling. All authors contributed to the writing of the manuscript.

Author information

Reprints and permissions information is available at www.nature.com/reprints. Readers are welcome to comment on the online version of the paper.

The authors declare no competing financial interests.

Data Availability Statement

The datasets generated during and/or analysed during the current study are available from the corresponding author on reasonable request.

Europe PMC Funders Author Manuscripts

We have followed two well-known strategies to enhance the thermal relaxation of an azobenzene: i) adding a push pull group or ii) forming a tautomerizable azo-hydrazone16. Correspondingly, we designed two polymerizable azoderivatives (Fig. 1, Extended data Fig. 1). The first molecule corresponds to a hydrogen bonded azopyridine (**I**) and the second one has a hydroxyl group at the ortho position (**II**). Each azo-derivative (7 mol. %) has been copolymerized with a mixture of a liquid crystal (LC) monoacrylate (RM23, 42 mol. %), an LC diacrylate (RM82, 50 mol. %) initiated by 1 mol. % of photoinitiator. The mixtures containing the compounds **I** and **II** will be further denoted as mixture **I** and mixture **II,** respectively. The monomer mixture has been aligned prior to polymerization in a splayed configuration over the cross-section of a thin film, with homeotropic alignment at one surface and planar alignment at the other. This splay-aligned configuration is chosen as it gives rise to the largest deformation in free standing films, as compared to uniaxial alignment, due to the opposite expansion/shrinkage behavior at the two sides of the LCN film as explored by Mol *et al.*17 and shown in the video S1.

The thermal relaxation of LCN films made of mixture **I** and mixture **II** has been studied by ultraviolet (UV)-spectroscopy and compared to LCNs containing: i) **A6MA,** a commonly used azobenzene for photoresponsive materials, ii) Disperse Red 1 acrylate (**DR1A**) a known commercial ultrafast azoderivatives, and iii) **AzoPy** corresponding to compound **I** without hydrogen bond. See Extended Data Fig. 2 and Extended Data Table 1 for the composition of the mixtures used and their thermal characterization.

As shown in Fig. 1, the half life time of the **A6MA** is long, typically over 1 hour while azoderivatives **I** and **II** exhibit a much faster relaxation, at room temperature. However, one should emphasize that temperature plays an important role in the relaxation process (Fig. 1 and Extended Data Fig. 3) and the half-life time drops below 1 s at 70 °C and 90 °C for **II** and **I**, respectively. Comparing **AzoPy** with compound **I** shows that the hydrogen bond enhances the push-pull effect, which results in a further decrease of the half life time. Finally, as predicted, the thermal relaxation of the **DR1A** is very fast; below 1 s at 30 °C. Furthermore, one can note that the cis-to-trans thermal relaxation of the azoderivatives follows a stretched exponential function as previously described for such glassy materials18–20.

With the intention to translate this fast molecular relaxation to the macroscopic deformation of the LCNs, small thin strips have been clamped at one end and exposed to UV-light. As previously reported, when **A6MA** is used, the film bends and remains in this position when the light is switched off. When **I** or **II** are used, both the bending and the relaxation are instantaneous as illumination is applied and removed. However, based on the molecular relaxation at room temperature, the time to full recovery is expected to be >10 min and ~1 min for **I** and **II**, respectively, which is far slower than the macroscopic observation. This can be explained by a significant increase of the film temperature of several tens of degrees during UV exposure. In the exposed films, temperatures reaching up to 85 °C have been recorded, which is above the glass transition (Tg) of the LCN, measured around 50 °C. At this temperature the half-life time drops to 2 s and <1 s for the compounds **I** and **II**, respectively. Besides, Pellerin *et al.* have recently shown that in the direct vicinity of the azobenzene molecules the temperature can reach values up to 228 °C21 and even higher

temperatures are calculated by Clark *et al.*22. Based on these findings it can be anticipated that molecular relaxation of the azobenzene moieties is faster because of the higher temperatures and hence even faster relaxation rates are expected.

In order to benefit from this fast relaxation, different sample configurations have been studied. When a strip of a thin LCN film made of mixture **I** is placed on a glass surface enabling free movement without further constraints, the polymeric film deforms in a caterpillar-like fashion. When the film is clamped at one end only, oscillations similar to the one reported by White *et al.* are observed6. Finally, when two edges of the film are glued together a tube is formed. Upon illumination the tube buckles and continuously deforms. Videos of those examples can be found in the ESI, video S2 (real-time).

More interestingly, when the same film, *i.e.* made from mixture **I,** is attached at both ends to a substrate and exposed to light (405 nm), a continuous travelling wave is initiated. As the distance between the two ends is shorter than the length of the strip, a buckled initial shape is created as shown in Fig. 2a. Turning on a fixed light source initiates a wave that continuously regenerates and propagates in a repeating, snake-like motion until the light is turned off. Similar results were obtained when using a film made of mixture **II** or by using **DR1A**, with its extremely short half-life time of 1.9 sec at 25 °C. However, when using an LCN containing **A6MA** , no continuous wave could be obtained due to a too slow thermal relaxation, see video S3. This suggests that the wave propagation is not restricted to the custom-made azo-derivatives and we anticipate that any molecule having a short half-life time is susceptible to give rise to such type of deformation. In the rest of this study, LCN films made with mixture **I** were used.

The use of a splay-aligned LCN gives an extra degree of control to the system and the direction of the wave is controlled by the film orientation with regard to the planar and homeotropic sides. As demonstrated in the cartoon of Fig. 2a, when the planar side is placed upwards, the induced wave propagates away from the light source; while when the homeotropic side is up, the wave propagates towards the light source. Videos S4 and S5 show this light-induced periodic wave motion for planar up and homeotropic up configurations, respectively. Videos are played in real time.

These two distinct wave trajectories are driven by the different photoactuation response of the two sides of the film. On illumination, the planar side shrinks strongly along the film’s long axis and expands weakly along the other two axes, inducing the light-exposed area to curve downwards. On illumination, the homeotropic side shrinks strongly along the film’s thickness and expands weakly along the other two axes, inducing the light-exposed area to curve upwards. Both types of deformation also induce slight curvature across the film’s short axis; as in a “slap band” bracelet, this slight deformation can produce mechanical instabilities such as snap-through transitions. As discussed further below, effects from self-shadowing produce a feedback loop enabling wave propagation and regeneration, as continuous displacement of the wave changes the position of the exposed/unexposed areas.

The speed of the displacement is greatly influenced by whether the planar or the homeotropic side is facing the light source. With the planar side towards the oblique

incoming light the wave travels in the direction towards the lamp with a frequency of 2.5 s^{-1}. When the film is flipped to put the homeotropic side up, the wave shows a slower frequency of 0.8 s^{-1} under the same exposure conditions, and the wave travels away from the light.

The incident angle between the light and the film is also found to influence the propagation speed of the generated waves. The wave propagates for angles ranging from 0° until 45° for the planar side up and from 0° to 15° for the homeotropic side up (Fig. 2b and Extended Data Fig. 4). Above these critical values the film becomes fully exposed, cancelling the self-shadowing effect. This working range of angles is valid for distances between the two attached points ranging from 2.2 cm to 1.6 cm for a film of initial length of 2.3 cm, *e.g.* buckled with end-to-end distance reduced up to 30 %. In the planar up configuration, a maximum speed is found for angles between 10° and 25°. Furthermore, the intensity of the light greatly influences the speed at which the wave travels. As shown in Fig. 2c, for a sample illuminated at an intensity of 510 $mW.cm^{-2}$ a frequency of 3 s^{-1} is reached. When the intensity is reduced to 230 $mW.cm^{-2}$ the frequency decreases to 0.5 s^{-1}. The motion stops entirely at light intensities below 175 $mW.cm^{-2}$, due to the photo-thermal effect. Indeed, for intensities below 150 $mW.cm^{-2}$ the temperature remains below the glass transition temperature (Extended Data Fig. 5a). A reference measurement with a uniaxial aligned film did not result in a wave deformation despite crossing the Tg upon illumination, see Extended Data Fig. 5b.

As mentioned above, temperature plays an important role as shown in Fig. 3. Upon exposure, the overall temperature of the film rises to roughly 50 °C. When the wave reaches the clamped end of the film, it arrests for a short period before a new wave forms and starts to propagate. During this very short instant, the temperature reaches values close to 100 °C (Fig.3 and Extended Data Fig. 6, videos S4 and S5). The significant heat generated also contributes to the deformation by thermal-expansion and is considered in the mechanism of creation and propagation of the wave.

To gain insight into the mechanism of this wave generation and its directionality, we have carried out a finite element elastodynamics analysis. We consider an LCN film with a “blueprinted” director field23, with the director homeotropic on one side and planar on the other with a linear gradient in between producing splay alignment, as shown in Fig. 2a. In simulations, the film is initially buckled into a curved shape, clamped at both ends on a solid substrate, then relaxed to mechanical equilibrium. We model incoming light as a plane wave from the left side of the sample at an angle of 10° above the horizontal. To determine which elements on the film surface are illuminated, incident light is represented as a grid of parallel rays and their first intersection with the surface is calculated. We model the film’s light-induced motion via a Hamiltonian-based elastodynamics algorithm with explicit time stepping. Our Hamiltonian-based model includes the film’s kinetic energy, elastic strain energy, and coupling between nematic order and mechanical strain23–25. Details of the simulation model are provided in the Methods section.

To model photoactuation, we make a rough approximation that the scalar order parameter S in each element along the surface decreases linearly in time when illuminated and increases linearly in time when shadowed, bounded by upper and lower limits. As S drops within a

volume element, coupling between nematic order and strain drives the material to shrink along the local director and expand in the two orthogonal directions. The S drop can either be caused by the isomerization of the azo units and the thermal expansion induced by the light exposure. Color indicates the magnitude of the scalar order parameter S, with blue and red regions showing the lowest and highest values, respectively as indicated in Fig. 2d and 2e.

Simulation results demonstrate the feedback mechanism that continuously generates waves. Consider first the planar side up configuration, shown in Fig. 2d. As light shines from the left and strikes the film, the local order parameter drops in the area shown in blue. There, the top surface of the film contracts along its long axis and the film curves downwards creating a bump just after the illuminated part. The resulting stress pushes the crest of the bump from the middle of the film toward the right, away from the incident light. When the crest approaches the clamped end, it arrests, and induced upward curvature in the blue region drives formation of a new wave crest to the left. Once the new crest grows to a critical size, it shadows the old crest which then disappears via a pop-through transition. This process repeats continuously as shown in Video S4.

Next consider the homeotropic side up configuration, also shown in Fig. 2e. In the illuminated region, the homeotropic material at the top of the film expands along both directions orthogonal to the surface normal, inducing upwards curvature. The resulting stress pulls the crest of the bump toward the left, towards the light source, where it arrests when it approaches the clamped end. The shadowed region relaxes back towards equilibrium, causing the crest to shrink until light passes over it and nucleates growth of a new crest to the right. There is a brief time delay while the new crest forms, followed by a pop-through transition where the old crest disappears and the new crest grows. This process repeats continuously as shown in Video S5.

Comparison of simulated trajectories with experimental observations, displayed in Videos S4 and S5, shows qualitative agreement. The simulations demonstrate that light-induced actuation, self-shadowing, and mechanical constraints are sufficient to create a feedback loop, producing wave generation driven by a constant light source. Additional simulations showed that pre-buckling the film and clamping it on a solid substrate are both necessary to enable the pop-through transition at the end of each cycle.

To demonstrate the versatility of the experimental system, a few examples have been developed where wave propagation is used to achieve light driven devices. Sand has been placed on the film, either before or during illumination, at the side of origin of the wave (Fig. 4a). While the wave develops, the sand is continuously transported towards the opposite side of the film. When energy is stored in the film, for instance when the weight of the sand inhibits wave propagation, the film will suddenly release the energy which ejects the sand far from the film. The film can be used many times without showing any damage or fatigue towards the sand or the light. In another example, the LCN film is challenged to carry uphill an object that is much heavier than its own weight and much bigger than its own dimension. The repeated propagation of the wave makes such operation possible by simultaneously pushing the object upwards and preventing it from sliding (video S6).

Finally, the most exceptional achievement obtained with the wave was the realization of a light-fueled self-propelled device. When the LCN is attached to a plastic frame as depicted in Fig. 4b, the device moves while the wave is travelling through the sample. The travelling direction is controlled by the orientation of the film as described previously, demonstrating directional light-induced locomotion. Small objects (few mg) can be attached to the frame and transported over large distances (cm). Videos of the light fueled device can be found in video S7 and S8. Videos are played in real time. We anticipate that the generation of the wave have potential applications in fields such as photomechanical energy harvesting, self-cleaning by contaminant rejection, and miniaturized transport of species in poorly accessible places.

Method

Synthesis of azoderivatives - Extended Data Fig.1

Synthesis of azopyridine (AzoPy), precursor of the compound **I**.

4-(4-hydroxyphenylazo)pyridine (ii):

4-(4-hydroxyphenylazo)pyridine was prepared according the procedure described by Naidek *et al.*26.

^{1}H NMR (400 MHz, [D_6]DMSO): δ = 10.64 (s, OH, 1H), 8.75 (d, *J* = 6 Hz, 2H), 7.86 (d, *J* = 9 Hz, 2H), 7.66 (d, *J* = 6 Hz, 2H), 6,98 (d, *J* = 9 Hz, 2H)

^{13}C NMR (100 MHz, [D_6]DMSO): δ = 162.76, 157.28, 151.72, 145.71, 126.25, 116.65, 116,26.

6-bromohexyl methacrylate (iii)

6-bromohexyl methacrylate was prepared according the procedure described by Stumpel *et al.*27. Only here acryloyl chloride was replaced by methacryloly chloride.

^{1}H NMR (400 MHz, $CDCl_3$): δ = 6.10 (s, 1H), 5.55 (s, 1H), 4.15 (t, *J* = 7 Hz, 2H), 3.41 (t, *J* = 7 Hz, 2H), 1.94 (s, 3H), 1.88 (p, *J* = 7 Hz, 2H), 1.70 (p, *J* = 7 Hz, 2H), 1,45 (m, 4H).

13C NMR (100 MHz, CDCl3): δ = 167.47, 136.46, 125.24, 64.52, 33.68, 32.62, 28.46, 27.80, 25.23, 18.33.

IR (ATR): $\bar{\nu}_{max}$ = 838, 937, 989, 1011, 1139, 1159, 1248, 1294, 1317, 1404, 1418, 1454, 1498, 1582, 1597, 1636, 1716, 2007, 2863, 2940.

4-(4-(6-methacryloxy)hexyloxyphenylazo)pyridine (AzoPy)

Compound **ii** (0.50 g, 2.5 mmol), **iii** (0.88 g, 2.75 mmol), K_2CO_3 (1.40 g, 10 mmol) and a grain of KI were suspended in 25 mL butanone under an argon atmosphere before the mixture was heated to reflux. After 15 h the mixture was cooled down and filtrated. 25 mL butanone was added to the filtrate. The filtrate was washed 3 times with 0.1 M KOH and once with brine. The organic layer was dried with $MgSO_4$, filtrated, and concentrated before

it was subjected to column chromatography (30 % EtOAc in heptane). Yield: 0.539 g (1.47 mmol, 59 %) orange solid.

^{1}H NMR (400 MHz, $CDCl_3$): δ = 8.77 (d, *J* = 6 Hz , 2H), 7.95 (d, *J* = 6 Hz, 2H), 7.01 (d, *J* = 11 Hz, 2H), 6.10 (s, 1H), 5.54 (s, 1H), 4.17 (t, *J* = 7 Hz, 2H), 4.06 (t, *J* = 6 Hz , 2H), 1.94 (s, 3H), 1.85 (p, *J* = 5 Hz, 2H), 1.71 (d, *J* = 7 Hz , 2H), 1.51 (m, 4H). See Extended Data Fig.7.

^{13}C NMR (100 MHz, $CDCl_3$): 167.52, 162.81, 157.44, 151.22, 146.74, 136.50, 125.61, 125.26, 116.16, 114.86, 68.27 64.59, 29.03, 28.56, 25.71, 18.35,

IR (ATR): $\bar{\nu}_{max}$ = 737, 838, 937, 989, 1011, 1139, 1159, 1248, 1294, 1317, 1404, 1418, 1454, 1498, 1597, 1636, 1715, 2007, 2862, 2940.

MS (MALDI-ToF): *m/z* = calc. $C_{21}H_{25}N_3O_3$+H^+ 368.20 $[M+H]^+$, found: 368.21.

Synthesis of compound **II**

(E)-4-((4-hydroxyphenyl)diazenyl)benzene-1,3-diol:

4-aminophenol (15 mmol, 1.6 g, 1 eq.) was suspended in water (4.1 mL). The reaction mixture was stirred and cooled to 0°C with an ice bath. Concentrated HCl (4.1 mL) was added dropwise. After 10 min of stirring, a solution of sodium nitrite (17 mmol, 1.14 g, 1.1 eq.) in water (3.5 mL) was added dropwise into the mixture. The solution was stirred for two hours at 0°C. Then, this solution was added dropwise over 2 hours to a solution of resorcinol (15 mmol, 1.6 g, 1 eq.) dissolved in water (3.5 mL) and NaOH (37.5 mmol, 1.5 g, 2.5 eq.) at 0°C. Stirring was continued for 3 hours while the mixture was warmed up to room temperature. The solution was acidified with 1M HCl and a red solid precipitated as the pure product with a yield of 85%.

^{1}H NMR (400 MHz, CD_3OD): 7.68 (d, *J* = 8.6 Hz, 2H), 7.63 (d, *J* = 9.0 Hz, 1H), 6.89 (d, *J* = 8.6 Hz, 2H), 6.48 (dd, *J* = 9.0 Hz, *J* = 2.3 Hz, 1H), 6.31 (d, *J* = 2.3 Hz, 1H).

^{13}C NMR (101 MHz, CD_3OD): δ 163.05, 161.18, 156.64, 145.30, 134.66, 133.44, 124.38, 116.94, 109.46, 104.01.

MS (MALDI-ToF): *m/z* = calc. $C_{12}H_{10}N_2O_3$+H^+: 231.08 $[M + H]^+$, found 231.03.

(E)-6-(4-((4-((6-(acryloyloxy)hexyl)oxy)-2-hydroxyphenyl)diazenyl)phenoxy)hexyl acrylate – compound **II:**

Trihydroxyazobenzene (0.43 mmol, 100 mg, 1 eq.), 6-bromohexylacrylate27 (0.86 mmol, 204 mg, 2 eq.), potassium carbonate (0.86 mmol, 120 mg, 2 eq.) and sodium iodide (catalytic amount) were suspended in DMF (5 mL) under an argon atmosphere and heated at 70°C overnight. The mixture was cooled down, filtered and concentrated under vacuum. Chloroform was added to the mixture and the organic layer was washed with saturated $NaHCO_3$ solution. The organic layer was dried over magnesium sulfate and concentrated. The crude mixture was subjected to chromatography column (5% methanol in chloroform). The wanted compound was obtained as an orange powder with a yield of 80%.

Europe PMC Funders Author Manuscripts

^{1}H NMR (400 MHz, $CDCl_3$): 13.68 (s, 1H), 7.77 (d, J = 8.8 Hz, 2H), 7.73 (d, J = 8.8 Hz, 1H), 6.97 (d, J = 8.8 Hz, 2H), 6.58 (dd, J = 8.8 Hz, J = 2.6 Hz, 1H), 6.40 (m, 3H), 6.12 (dd, J = 17.3 Hz, J = 10.4 Hz, 2H), 5.82 (dd, J = 10.4 Hz, J = 1.5 Hz, 2H), 4.18 (m, 4H), 4.02 (m, 4H), 1.83 (m, 4H), 1.72 (m, 4H), 1.50 (m, 8H). See Extended Data Fig.7.

^{13}C NMR (101 MHz, $CDCl_3$): δ 166.46, 162.82, 161.08, 155.76, 144.46, 134.16, 132.79, 130.69, 128.72, 123.45, 115.11, 108.28, 101.99, 68.33, 68.29, 64.64, 29.22, 29.11, 28.70, 25.88, 25.86.

MS (MALDI-ToF): m/z = calc. $C_{30}H_{38}N_2O_7$+H^+: 539.28 $[M + H]^+$, found 539.32.

Mixture and film preparation

The **AzoPy** was mixed with 6OBA (4-((6-(acryloyloxy)hexyl)oxy)benzoic acid, custom made by Synthon Chemicals) in an equimolar ratio in order to form a supramolecular diacrylate. The molecules were dissolved in hot ethanol, upon cooling compound **I**, precipitates.

In order to form the LCN based on compound **I**, 9 mg (7 mol %) of compound **I**, 61 mg (50 mol %) of RM82 and 30 mg (42 mol %) of RM 23 were dissolved in dichloromethane and subsequently the solvent was evaporated. To prepare the LCN based on compound **II**, 63 mg (50 mol.%) of RM82, 30mg (42 mol.%) of RM23 and 7 mg (7 mol.%) of the azoderivative **II**, were used in order to have similar cross link density and similar molar amount of azo compound. The equivalent of 1wt% of photoinitiator, Irgacure 819, was also added in order to perform photopolymerization.

Homemade cells were prepared by gluing together a glass plate coated with polyimide and rubbed with a clean uncoated but treated with ozone glass plate. The spacing was chosen to be 20 μm and fixed using glass bead of the respective diameter. Consequently all the LCN used for macroscopic deformation have a thickness of 20 μm.

The cells were filled by capillary action at 95 °C, where the mixtures are isotropic. Once the cells were totally filled, the temperature was decreased to reach the nematic phase, at 80 °C. The polymerization was performed at this temperature for about 45 min, with an Exfo Omnicure S2000 equipped with a 320 nm – 500 nm filter. The light intensity during the polymerization is about 50 ± 15 $mW.cm^{-2}$. A 405 nm or 455 nm cut off filter was used with **I** and **II** respectively, in order to prevent premature isomerization of the azobenzene. After photopolymerization the film was post cured at 130 °C for 10 min and slowly cooled down to room temperature.

DSC was performed on both the mixture and the polymerized films (TA instrument Q1000). The results are presented in the extended data figure 2. The maximum absorption was determined using a spectrophotometer shimadzu UV-31020.

The film were peeled off and cut in the desired shape, using a razor blade. Typically the films were cut as long strips (2.3 cm x 4 mm) with the alignment director of the molecule parallel to the long edge.

Actuation

The azoderivative containing films were actuated using 405 nm LED light (ThorsLab) mounted with a collimator. The UV intensity at the focus point was 510 $mW.cm^{-2}$. The films were either unclamped, clamped at one side or taped at both ends. The deformations were recorded with a camera and further treated with image analysis software.

The sample used to measure the frequencies in figure 2 are 23mm long, 4 mm wide and 20μm thick. The end are fixed at 2.2 cm or 1.7 cm appart using tape which produces a pre-set curvature. The illumination is fixed and comes from the left side.

To create the device presented in figure 4c and 4d, the film is stuck to a passive frame. The passive frame applies a mechanical constraint, allowing the wave to propagate. Locomotion is driven by self-shadowing effects that produce a feedback loop.

Characterization techniques

The mesophases of the mixtures as well as the alignment of the LCNs were verified using polarized optical microscopy (POM). The equipment used was a Leica D300.

The thermal properties (Tg) of the LCNs were determined with differential scanning calorimetry. The apparatus used was a TAinstrument Q1000. Three cycles from -50 °C until 150 °C at a rate of 10 $°C.min^{-1}$ were performed.

The transmission spectrum were recorded with a uv-spectrophotometer (Shimadzu UV-3102). Transmission is measured to ensure that light is going throughout the overall thickness of the films. See Extended Data Fig.8.

The isomerization kinetic of the two azoderivatives were characterized with a uv-spectrophotometer (Shimadzu UV-3102) in a kinetic mode.Measurements were recorded after a 1 min exposure to light of a wavelength that corresponds to the absorbance maximum, *i.e.* 365, 365, 405, and 470 nm for the films containing **A6MA**, **I**, **II**, and **DR1A**, respectively The relaxation was monitored by following the absorbance at the respective wavelength with a measurement done every 1 second (limit of the instrument). The absorbance couldn't be measured during the exposure to 365 nm LED light since the detector was over-saturated with the illuminating light. The first measurement was done within the first second after switching off the UV light which gives a certain error on the precision of measurement especially when characterizing fast relaxation. Films having a thickness of 5 μm were used to perform the photochemical properties.Thicker samples resulted in a too high absorbance.

The relaxation kinetic were fitted with a stretched–exponential function described by the equation : $A(t) = A_\infty - (A_\infty - A_0)e^{-(k.t)^\beta}$. The stretch exponent parameter β being 0.60 ± 0.05, 0.34 ± 0.02, 0.72 ± 0.03, 0.49 ± 0.12 and 0.44 ± 0.11 for **A6MA**, **DR1A**, **AzoPy**, **I** and **II** respectively. Since for the normalized data $A_\infty = 0$ and $A_0 = -1$, the half-life time can be written as: $\tau = \frac{\sqrt[\beta]{\ln(2)}}{k}$.

Europe PMC Funders Author Manuscripts

Finite Element Elastodynamics Simulation

We model a nematic elastomer thin film discretized in a three-dimensional tetrahedral mesh with 5717 nodes and 19478 tetrahedral volume elements, with physical dimensions 1.5 cm x 0.1 cm x 250 microns. The nematic director ***n*** within each element represents the splayed "blueprinted" structure present in the material, with a gradient from planar on one surface to homeotropic on the other. The scalar order parameter S in each element varies with time as described below. Light-driven mechanical response is modeled via the Hamiltonian:

$$H=\frac{1}{2}\sum_t V^t C_{ijkl}\varepsilon_{ij}^t\varepsilon_{kl}^t-\alpha\sum_t V^t\varepsilon_{ij}^t\left(S^t-S_o\right)\frac{1}{2}\left(3n_i^t n_j^t-\delta_{ij}\right)+\frac{1}{2}\sum_p m_p v_p^2$$

Here the first term is the elastic strain energy summed over elements t, where ε_{ij} is the Green-Lagrange strain, C_{ijkl} is a tensor of elastic constants, and V^t is the volume of element t in its reference state. The second term is the potential energy due to coupling of strain and nematic order with a coupling coefficient α. Here S^t is the instantaneous nematic scalar order parameter in element t, and S^0 is the value in the fully relaxed nematic state. The last term represents kinetic energy using the lumped mass approximation, with mass m_p and instantaneous velocity v_p of each node p. The coupling coefficient α is set such that a unixially aligned sample shrinks in length by 44% when fully switched from nematic to isotropic.

Material density was set at 1.2 g.cm^{-3} in accord with experimental measurements. The elastic constants used in the simulation are Poisson ratio of 0.49 and Young's modulus 3.4 MPa. While we might expect the material to have Poisson ratio closer to the incompressible limit of 0.5, we used a reduced value to improve the numerical stability of the dynamics simulation. The computational mesh we used for our finite element simulations has a length to thickness aspect ratio of 60, which is not as extreme as the film in the experimental system which has a length to thickness ratio of 1000. Since the bending energy scales as film thickness cubed, we used a softer Young's modulus in the simulation so the bending energy is still of the right order of magnitude.

To model photoactuation in the sample with splay geometry, the local scalar order parameter S in each element evolves as a function of time according to its exposure to light. We make the simplifying assumption that for illuminated surface elements, S decreases linearly in time, while for those in shadow, S increases linearly in time. In both cases S is bounded by upper and lower limits which refer respectively to the fully relaxed nematic state and the maximally disordered illuminated state. The selected rate of change for S allows full transition in less than one second in each direction.

The effective force on each node is calculated as the derivative of the total potential energy with respect to node displacement. Every node experiences an effective force contribution from each tetrahedral element it touches, and these are summed vectorwise at each time step. Node equations of motion are integrated using the Velocity Verlet algorithm with new forces calculated at each time step, while clamped nodes at the ends of the film are held fixed. The

optics calculation to determine which parts of the film's top surface are illuminated is also repeated at each time step.

The substrate below the film is modelled as an infinitely hard/smooth surface, and collisions between the film and the substrate are treated as inelastic.

Dissipative forces proportional to node momentum are added to approximate the effects of air resistance. The finite element simulation suggests that kinetic energy plays a key role in the shape response. If we increase the amount of dissipation (drag) in the finite element simulation above a threshold value, then wave motion fails to initiate.

The simulation code is implemented for GPU acceleration. Using a time step of 2×10^{-5} seconds, and duration 2×10^{6} time steps requires about 25 minutes to execute on a single GPU-equipped processor, modeling a total of 40 seconds of motion.

The finite element simulation model does not take into consideration the temperature dependence of the material's elastic moduli or the effects of thermal expansion. These effects may be explored in future more detailed modeling efforts, but the present simulation demonstrates that they are not essential to generate perpetual wave motion.

Europe PMC Funders Author Manuscripts

Europe PMC Funders Author Manuscripts

Extended Data

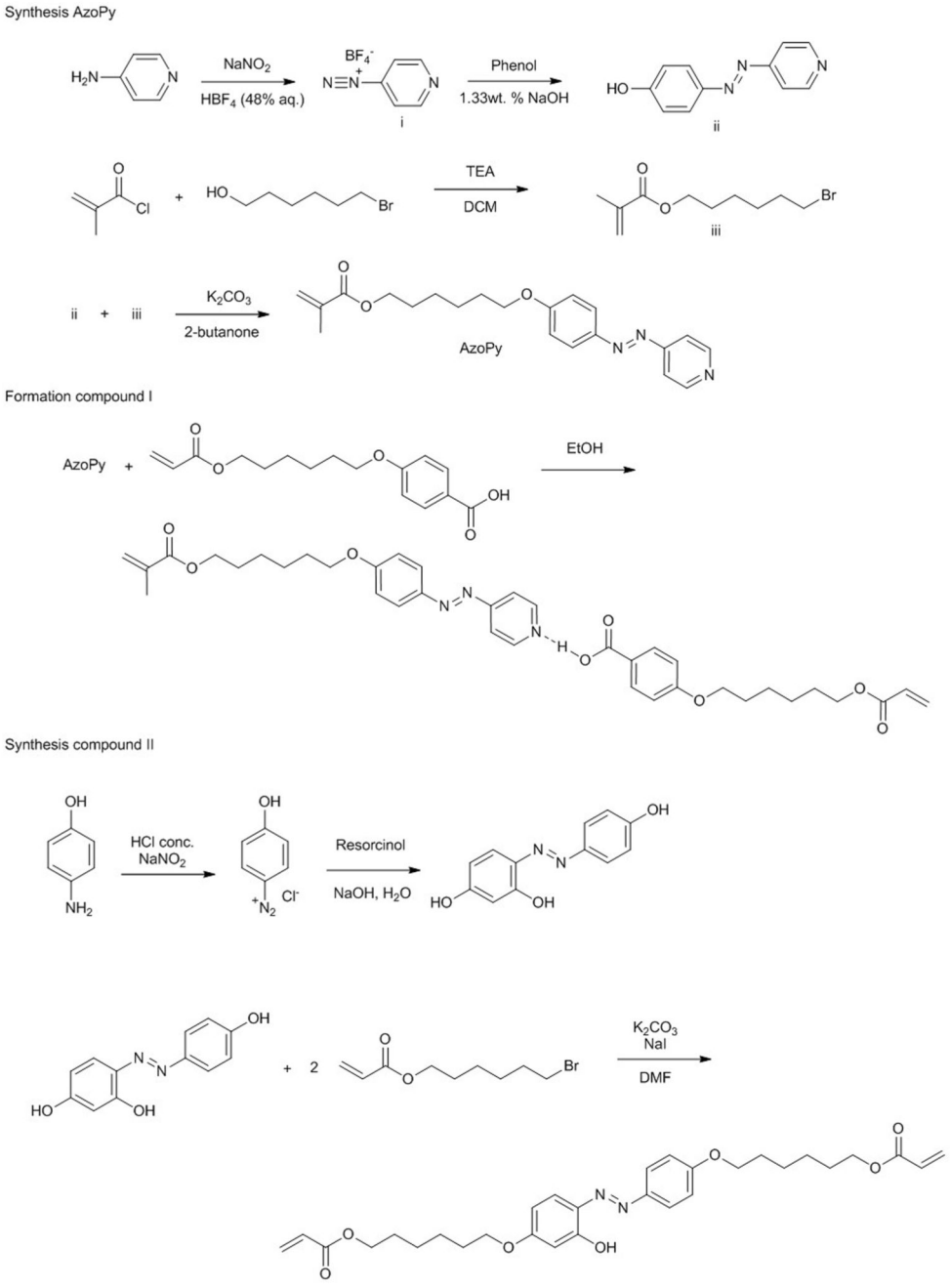

Extended data Figure 1. Synthetic routes for constituent compounds.

Components of the LCN films include **AzoPy**, compound **I** and compound **II**.

Europe PMC Funders Author Manuscripts

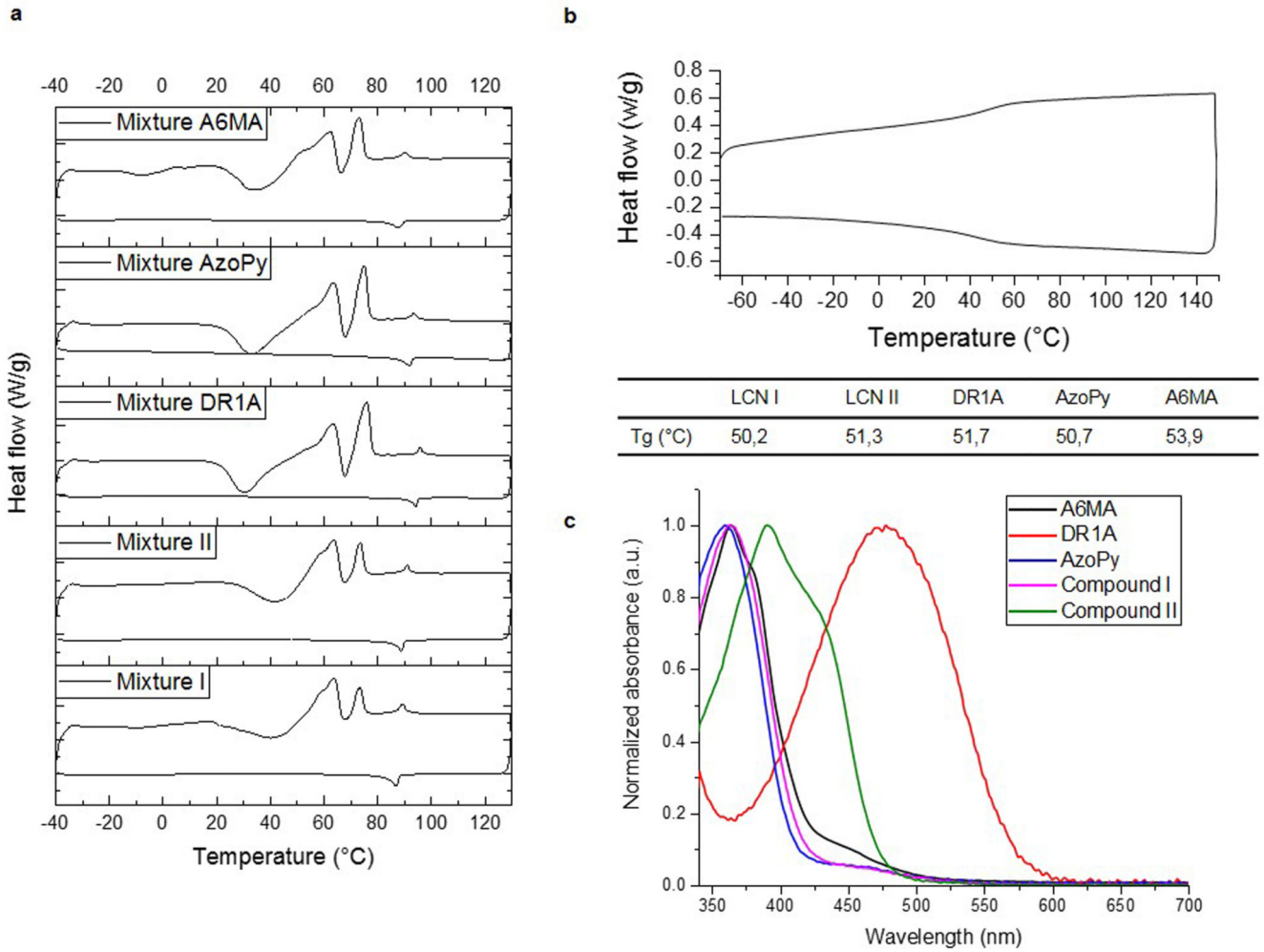

	LCN I	LCN II	DR1A	AzoPy	A6MA
Tg (°C)	50,2	51,3	51,7	50,7	53,9

Extended data Figure 2. Thermal characterization of the mixtures used in the study.

a, Differential Scanning Calorimetry (DSC) scans (second runs, exotherm downwards) showing the phase behavior of all mixtures investigated. The nematic to isotropic transition occurs at 90°C. **b**, DSC scan of a polymerized sample showing the change in specific heat at the glass transition temperature (Tg). The table summarizes the Tg data of the various polymerized compositions. **c**, Normalized absorption spectra of the various mixtures investigated.

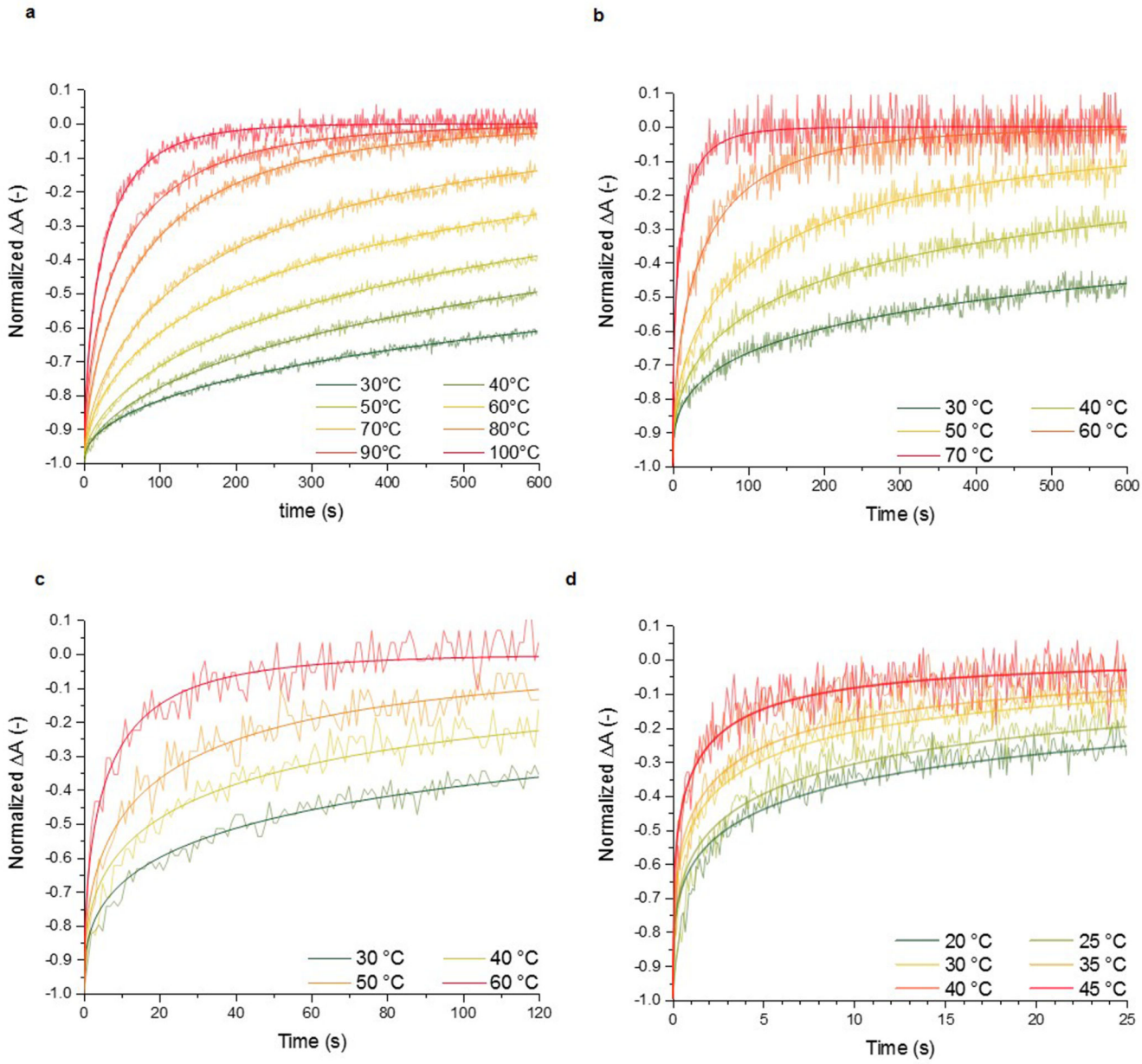

Extended data Figure 3. Relaxation kinetics of the azo-derivatives embedded in the LCN.
Thermal relaxation from the photostationary cis state to the trans state of (**a**) **A6MA**, (**b**) compound **I**, (**c**) compound **II**, and (**d**) **DR1A** at various temperatures.

Europe PMC Funders Author Manuscripts

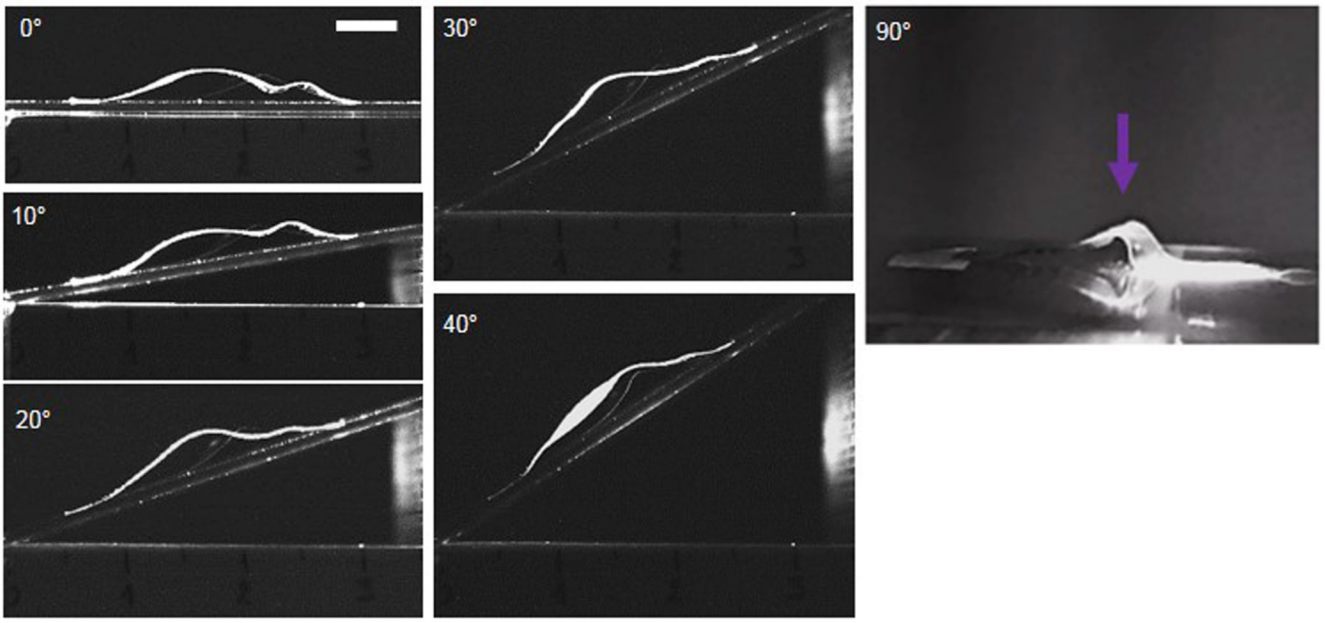

Extended data Figure 4. Pictures taken at different angles showing the created curvatures inducing the shadow effect.

Scale bar: 5 mm. At 90°, the bump is formed but since no shadow is created the wave cannot propagates and the film remains in that position.

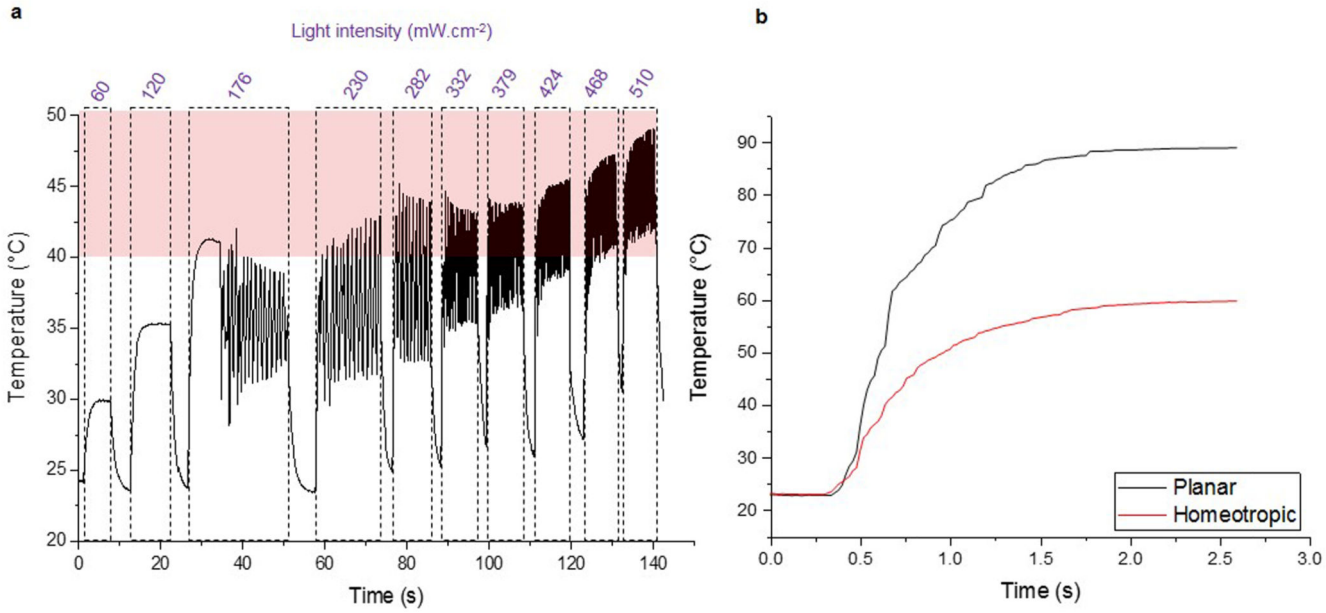

Extended data Figure 5. Temperature measured at the front of the wave.

a, Influence of the intensity on the temperature increase at the front of the wave. The red layer helps to visualize the glass transition region. **b,** Temperature measured for the uniaxial oriented sample. despite the rubbery character of the films, no motion was observed.

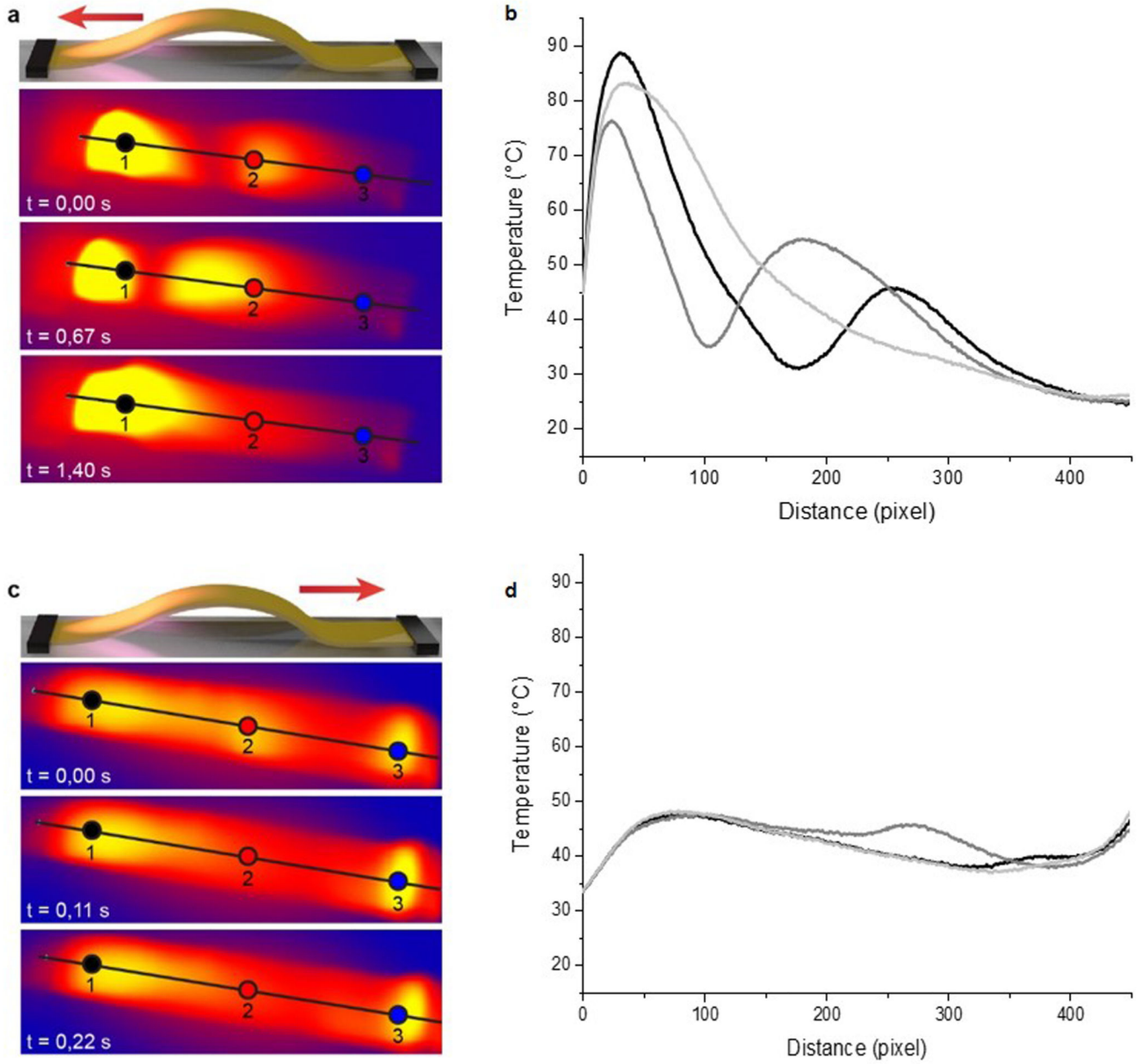

Extended data Figure 6. Temperature measurements during wave propagation.

a,c, Thermal pictures of the wave taken at different time. **b,** Temperature profile over the length of the film during wave propagation at $t = 0$ s (black line), $t = 0.67$ s (dark gray line and $t = 1.40$ s(light gray line). **d,** Temperature profiles for the planar up sample at $t = 0$ s (black line), $t = 0.11$ s (dark gray line) and $t = 0.22$ s (light gray line).

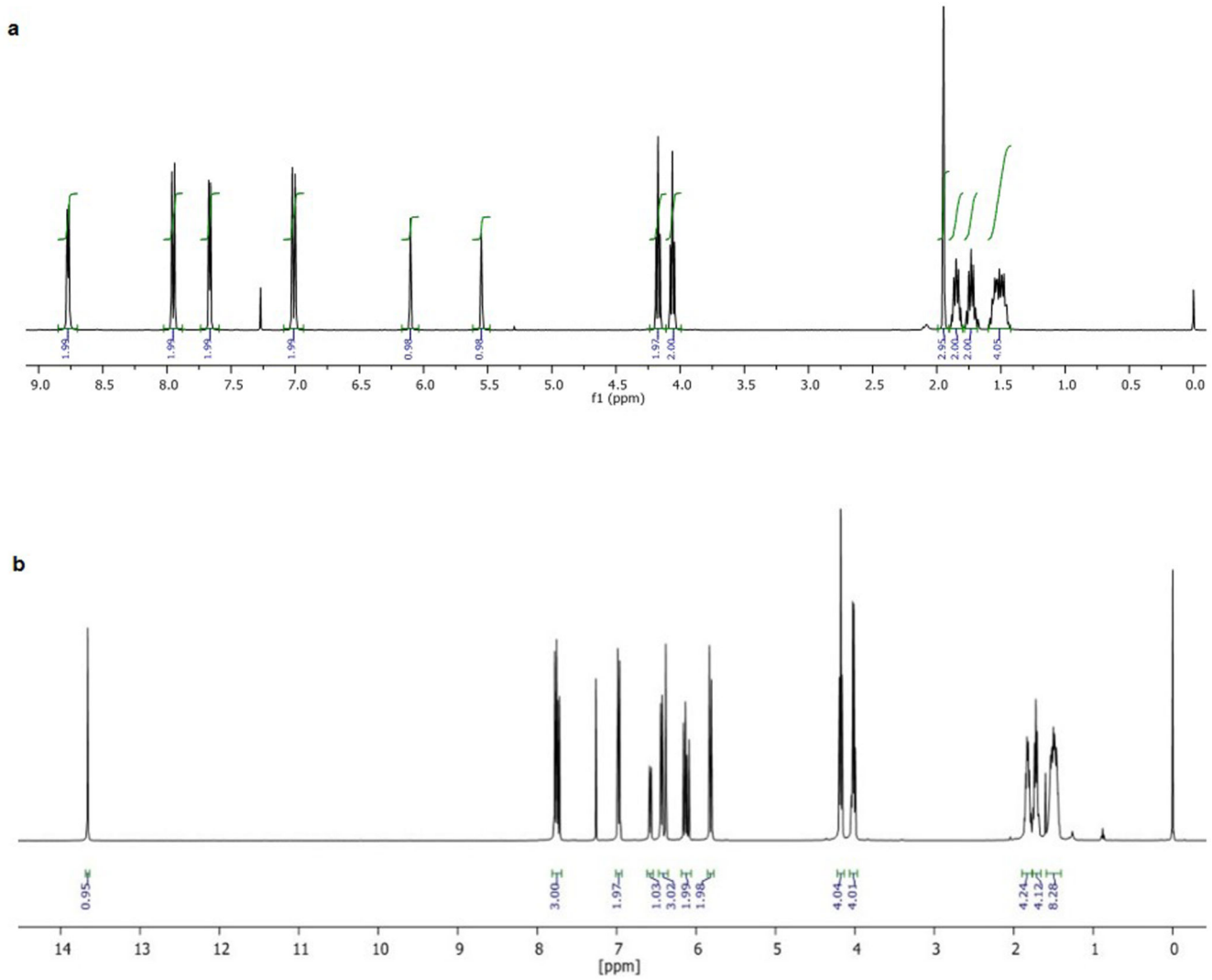

Extended data Figure 7. ^{1}H-NMR spectra of constituent compounds.
a, ^{1}H-NMR of the compound AzoPy used to form the compound **I**. **b,** ^{1}H-NMR of the compound **II**.

Europe PMC Funders Author Manuscripts

Europe PMC Funders Author Manuscripts

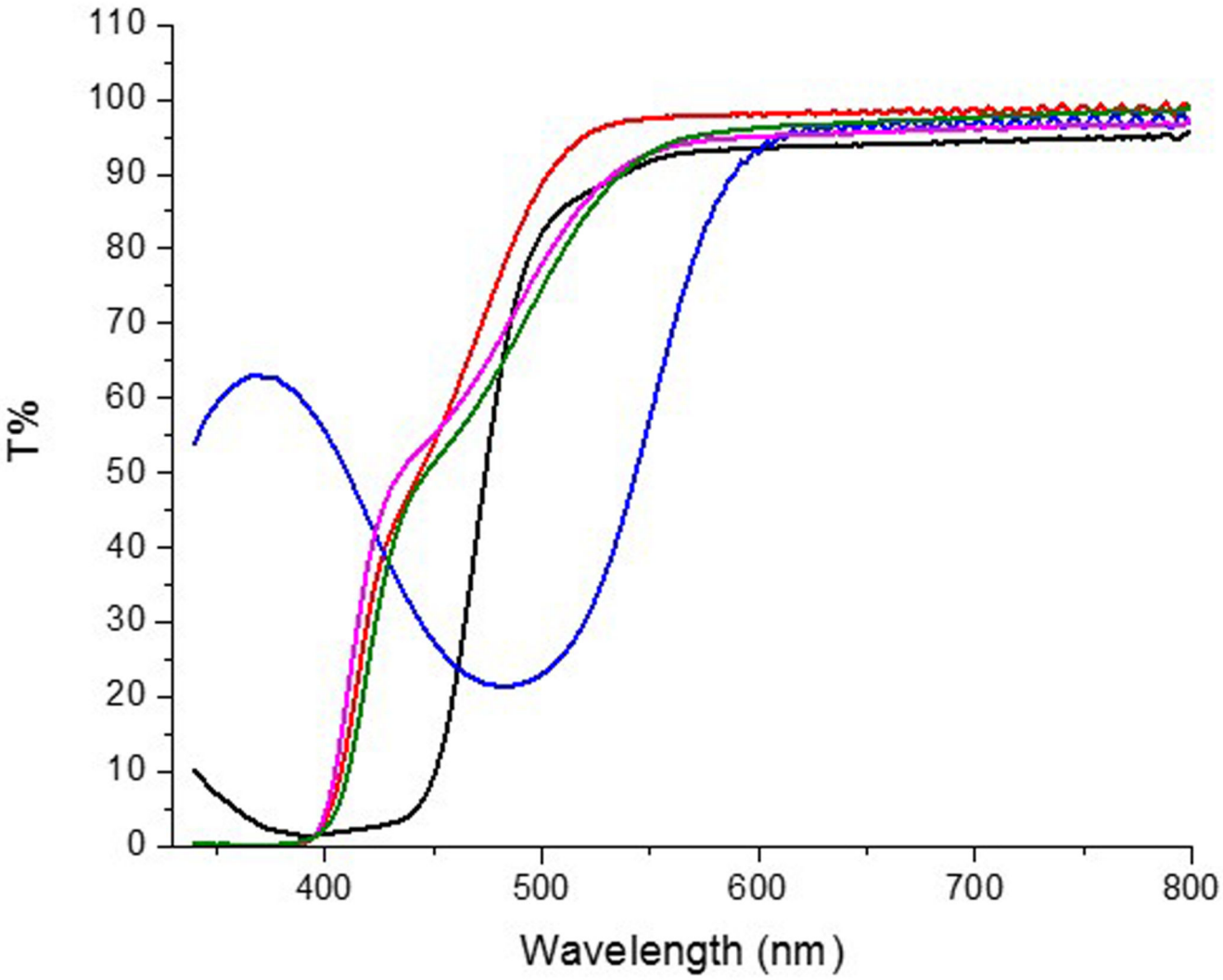

Extended data Figure 8. Transmission spectra of LCN films.

compound **I** (green), **II** (black), **A6MA** (red), **AzoPy** (pink) and **DR1A** (blue). Thickness 20μm. The films containing **A6MA**, **I** and **AzoPy** are actuated with 405nm light. At that wavelength the transmission are 6.3 %, 8.9 % and 4.1 % for **A6MA**, **AzoPy** and **I**, respectively. The samples containing **DR1A** and **II** are illuminated with a 455 nm light. At this wavelength the initial transmission is 13 % and 26 % for **II** and **DR1A** respectively.

Extended Data Table 1
Chemical composition of the mixture used.

Mixture containing **DR1A**, has a slightly different composition because the extinction coefficient of **DR1A** is higher than the previous molecules. Consequently the amount of RM 23 and RM82 are also adjusted to maintain similar quantity of crosslinker. Both the molar ratio (mol.%) and the corresponding amount (mg) are reported.

	Mixture with AzoPy	Mixture with I	Mixture with II	Mixture with A6MA	Mixture with DR1A
AzoPy	7 mol.% 5 mg	/	/	/	/
Compound I	/	7 mol.% 9 mg	/	/	/
Compound II	/	/	7 mol.% 7 mg	/	/
A6MA	/	/	/	7 mol.% 7 mg	/
DR1A	/	/	/	/	7 mol.% 1 mg
RM82	57 mol.% 70 mg	50 mol.% 61 mg	50 mol.% 63 mg	51 mol.% 63 mg	57 mol.% 70 mg
RM23	35 mol.% 25 mg	42 mol.% 30 mg	41 mol.% 30 mg	41 mol.% 30 mg	41 mol.% 29 mg
Irgacure 819	1 mol.% 1 mg	1 mol.% 1 mg	1 mol.% 1 mg	1 mol.% 1 mg	1 mol.% 1 mg

Supplementary Material

Refer to Web version on PubMed Central for supplementary material.

Acknowledgements

This work was financially supported by the Netherlands Organization for Scientific Research (NWO – TOP PUNT Grant: 10018944), the European Research Council (Vibrate ERC, Grant 669991), and the US National Science Foundation Grants DMR- 1409658 and CMMI- 1436565. A.H.G. acknowledges the funding from the People Programme (Marie Curie Actions) of the European Union's Seventh Framework Programme FP7-2013, Grant No. 607602. Computing resources provided by the Ohio Supercomputer Center (M.V., A.K., RLBS) RLBS acknowledges F. Nazarov for helpful discussions and B. L. Mbanga for his key role in developing the FEM algorithm. The work of DJM forms part of the research programme of the Dutch Polymer Institute (DPI), project 776n.

References

1. Tabata O, Hirasawa H, Aoki S, Yoshida R, Kokufuta E. Ciliary motion actuator using self-oscillating gel. Sens Actuators Phys. 2002; 95:234–238.
2. Murase Y, Maeda S, Hashimoto S, Yoshida R. Design of a Mass Transport Surface Utilizing Peristaltic Motion of a Self-Oscillating Gel. Langmuir. 2009; 25:483–489. [PubMed: 19063637]
3. Maeda S, Hara Y, Yoshida R, Hashimoto S. Peristaltic Motion of Polymer Gels. Angew Chem Int Ed. 2008; 47:6690–6693.
4. Maeda S, Hara Y, Sakai T, Yoshida R, Hashimoto S. Self-Walking Gel. Adv Mater. 2007; 19:3480–3484.
5. Martinez A, Smalyukh II. Light-driven dynamic Archimedes spirals and periodic oscillatory patterns of topological solitons in anisotropic soft matter. Opt Express. 2015; 23:4591. [PubMed: 25836496]

6. White TJ, et al. A high frequency photodriven polymer oscillator. Soft Matter. 2008; 4:1796.
7. Yu Y, Nakano M, Ikeda T. Photomechanics: Directed bending of a polymer film by light. Nature. 2003; 425:145–145. [PubMed: 12968169]
8. van Oosten CL, Harris KD, Bastiaansen CWM, Broer DJ. Glassy photomechanical liquid-crystal network actuators for microscale devices. Eur Phys J E. 2007; 23:329–336. [PubMed: 17687511]
9. Li M-H, Keller P, Li B, Wang X, Brunet M. Light-Driven Side-On Nematic Elastomer Actuators. Adv Mater. 2003; 15:569–572.
10. Iamsaard S, et al. Conversion of light into macroscopic helical motion. Nat Chem. 2014; 6:229–235. [PubMed: 24557138]
11. Yamada M, et al. Photomobile Polymer Materials: Towards Light-Driven Plastic Motors. Angew Chem Int Ed. 2008; 47:4986–4988.
12. Bandara HMD, Burdette SC. Photoisomerization in different classes of azobenzene. Chem Soc Rev. 2012; 41:1809–1825. [PubMed: 22008710]
13. García-Amorós J, Velasco D. Recent advances towards azobenzene-based light-driven real-time information-transmitting materials. Beilstein J Org Chem. 2012; 8:1003–1017. [PubMed: 23019428]
14. van Oosten CL, Bastiaansen CWM, Broer DJ. Printed artificial cilia from liquid-crystal network actuators modularly driven by light. Nat Mater. 2009; 8:677–682. [PubMed: 19561599]
15. Camacho-Lopez M, Finkelmann H, Palffy-Muhoray P, Shelley M. Fast liquid-crystal elastomer swims into the dark. Nat Mater. 2004; 3:307–310. [PubMed: 15107840]
16. Brode WR, Gould JH, Wyman GM. The Relation between the Absorption Spectra and the Chemical Constitution of Dyes. XXV. Phototropism and cis-trans Isomerism in Aromatic Azo Compounds 1. J Am Chem Soc. 1952; 74:4641–4646.
17. Mol GN, Harris KD, Bastiaansen CWM, Broer DJ. Thermo-Mechanical Responses of Liquid-Crystal Networks with a Splayed Molecular Organization. Adv Funct Mater. 2005; 15:1155–1159.
18. Mita I, Horie K, Hirao K. Photochemistry in polymer solids. 9. Photoisomerization of azobenzene in a polycarbonate film. Macromolecules. 1989; 22:558–563.
19. Poutanen M, Ikkala O, Priimagi A. Structurally Controlled Dynamics in Azobenzene-Based Supramolecular Self-Assemblies in Solid State. Macromolecules. 2016; acs.macromol.6b00562. doi: 10.1021/acs.macromol.6b00562
20. Serra F, Terentjev EM. Effects of Solvent Viscosity and Polarity on the Isomerization of Azobenzene. Macromolecules. 2008; 41:981–986.
21. Vapaavuori J, Laventure A, Bazuin CG, Lebel O, Pellerin C. Submolecular Plasticization Induced by Photons in Azobenzene Materials. J Am Chem Soc. 2015; 137:13510–13517. [PubMed: 26439981]
22. Fang GJ, et al. Athermal photofluidization of glasses. Nat Commun. 2013; 4:1521. [PubMed: 23443549]
23. Sawa Y, et al. Shape and chirality transitions in off-axis twist nematic elastomer ribbons. Phys Rev E. 2013; 88:022502.
24. Konya A, Gimenez-Pinto V, Selinger RLB. Modeling Defects, Shape Evolution, and Programmed Auto-Origami in Liquid Crystal Elastomers. Front Mater. 2016; 3
25. de Haan LT, et al. Accordion-like Actuators of Multiple 3D Patterned Liquid Crystal Polymer Films. Adv Funct Mater. 2014; 24:1251–1258.
26. Naidek KP, et al. Ruthenium Acetate Cluster Amphiphiles and Their Langmuir-Blodgett Films for Electrochromic Switching Devices. Eur J Inorg Chem. 2014; 2014:1150–1157.
27. Stumpel JE, Liu D, Broer DJ, Schenning APHJ. Photoswitchable Hydrogel Surface Topographies by Polymerisation-Induced Diffusion. Chem - Eur J. 2013; 19:10922–10927. [PubMed: 23821576]

Europe PMC Funders Author Manuscripts

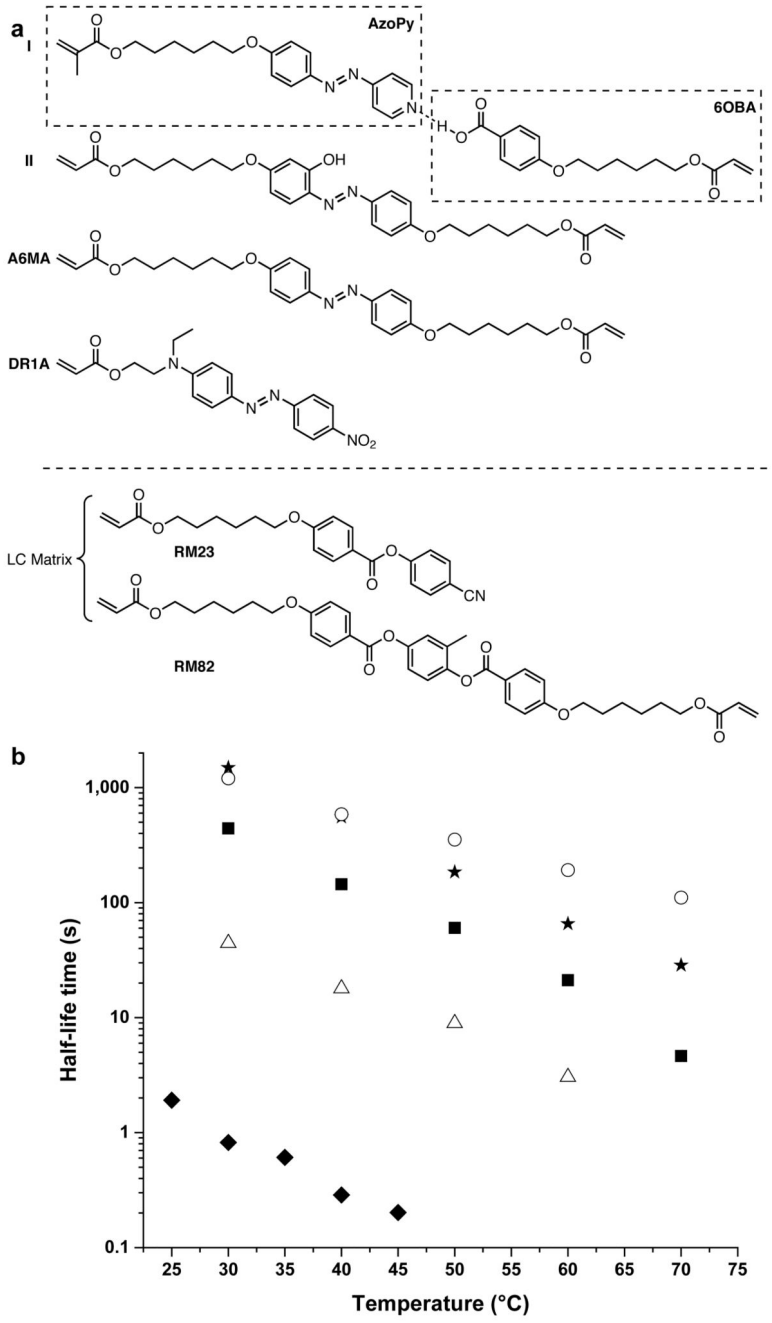

Figure 1. Azo dyes and their cis to trans relaxation

a, Chemical structures of azo-derivatives and liquid crystal mesogens. **b,** Exponential decrease of their half-life time as a function of temperature. Circle, square, triangle star and diamond for the **A6MA**, **I**, **II**, **AzoPy** and **DR1A**, respectively.

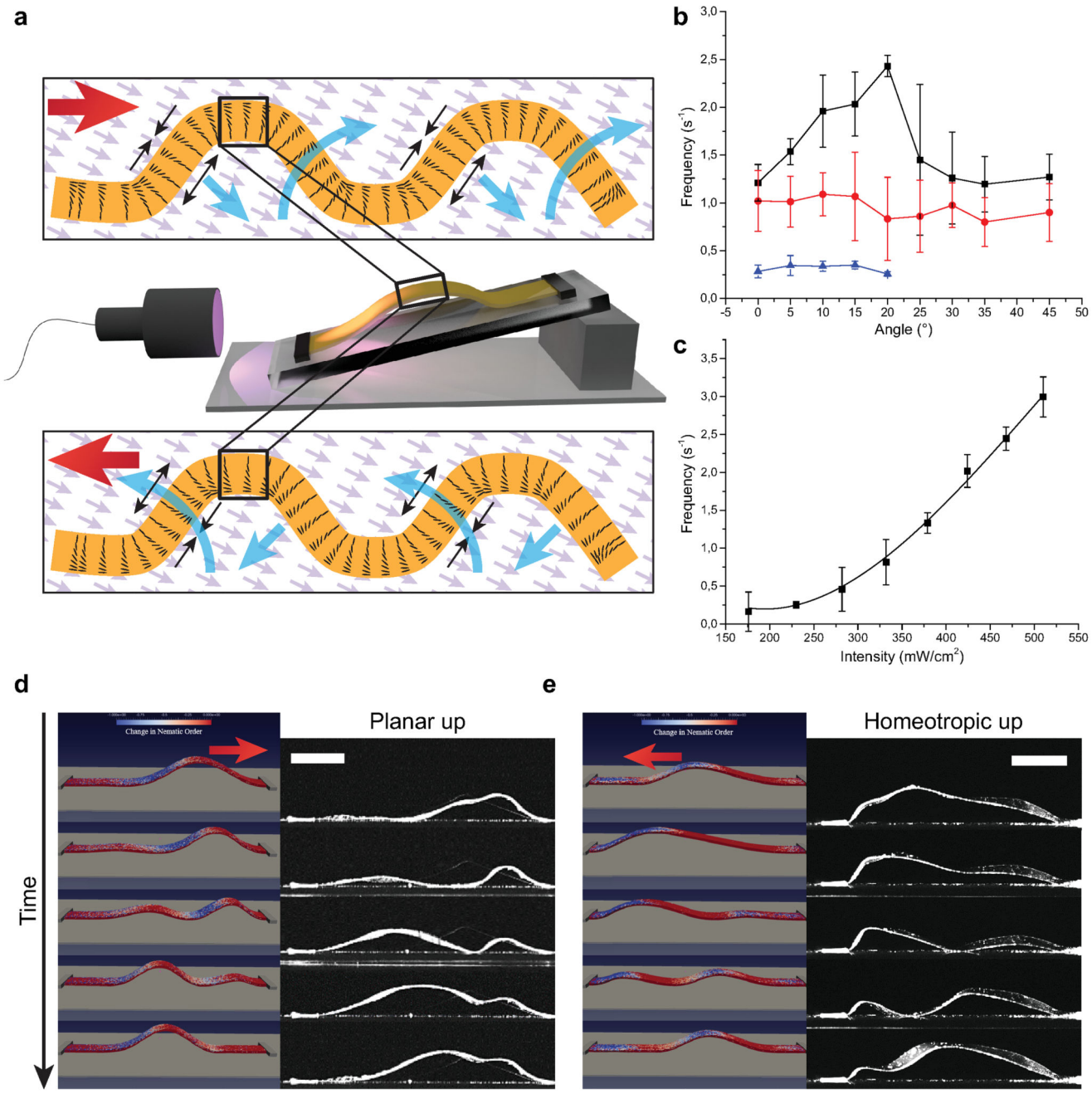

Figure 2. Mechanism of wave propagation and parameters that influence propagation speed

a, Experimental set-up, schematic. **b**, Frequency versus incident light angle. Planar side up, distance end-to-end L=22 mm (black) and 17 mm (red) and homeotropic side up, L=22 mm (blue). Error bar: s.d. n= 3. **c**, Influence of light intensity on wave velocity. Planar side up, L= 22 mm. **d, e,** Comparison of simulation (left) and experimental data (right) for both planar (**d**) and homeotropic (**e**) side up (video S4 and S5). Incident light: 10° from the left, L=22 mm. Scale bar: 5 mm. Films made of mixture I, size 23 mm x 4 mm x 20μm.

Europe PMC Funders Author Manuscripts

Europe PMC Funders Author Manuscripts

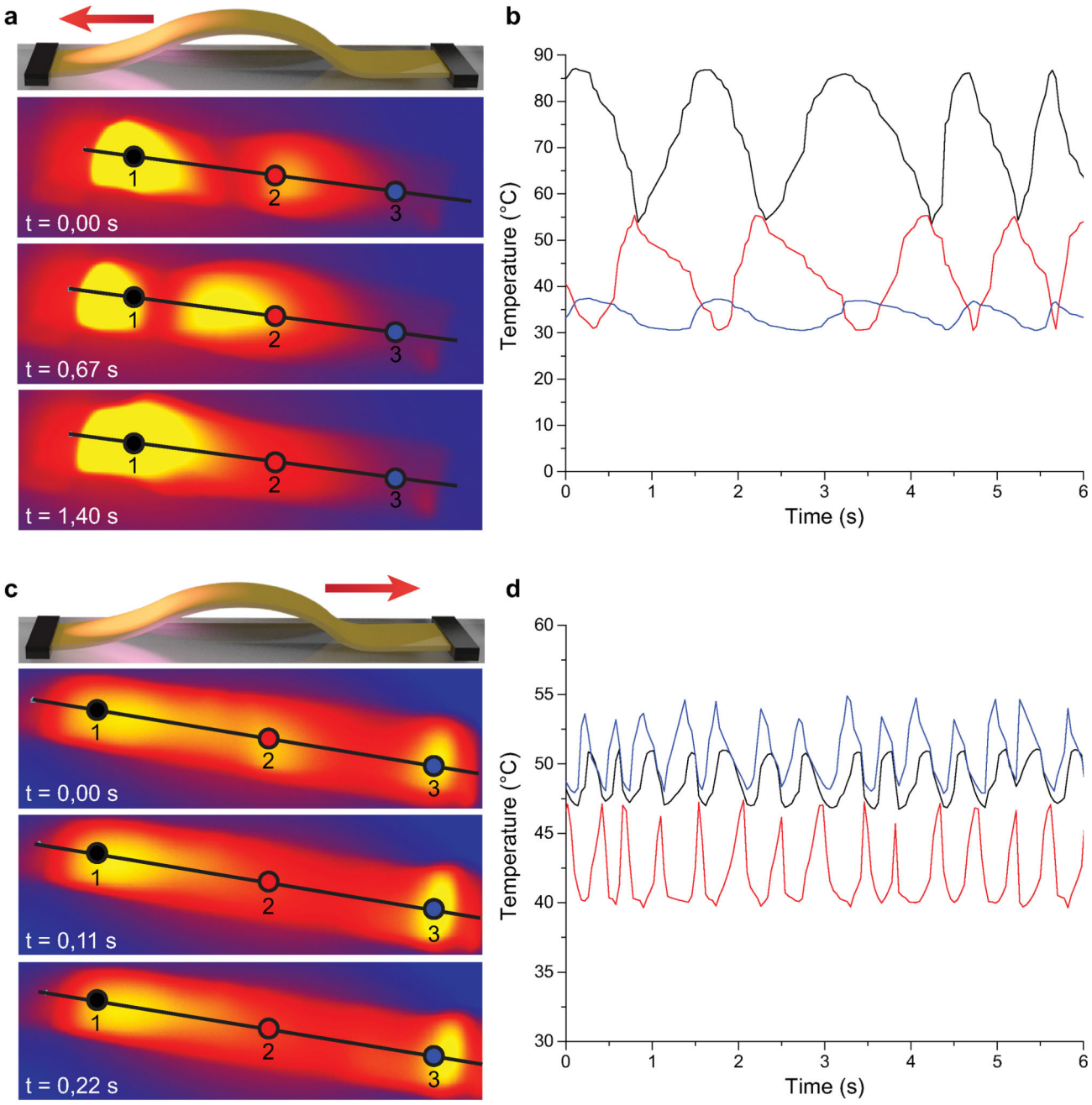

Figure 3. Temperature traces recorded by an IR-thermal camera during wave propagation

Mixture **I** based LCN films exposed to UV-light (500 mW.cm^{-2}). **a, b,** Temperature profiles during exposure at the homeotropic side and **c, d,** at the planar side. **a, c,** Local hot spots. **b, d**, Oscillating temperatures at positions 1 (black), 2 (red) and 3 (blue) as indicated in **a** and **c**. Distance end-to-end: 22 mm.

Europe PMC Funders Author Manuscripts

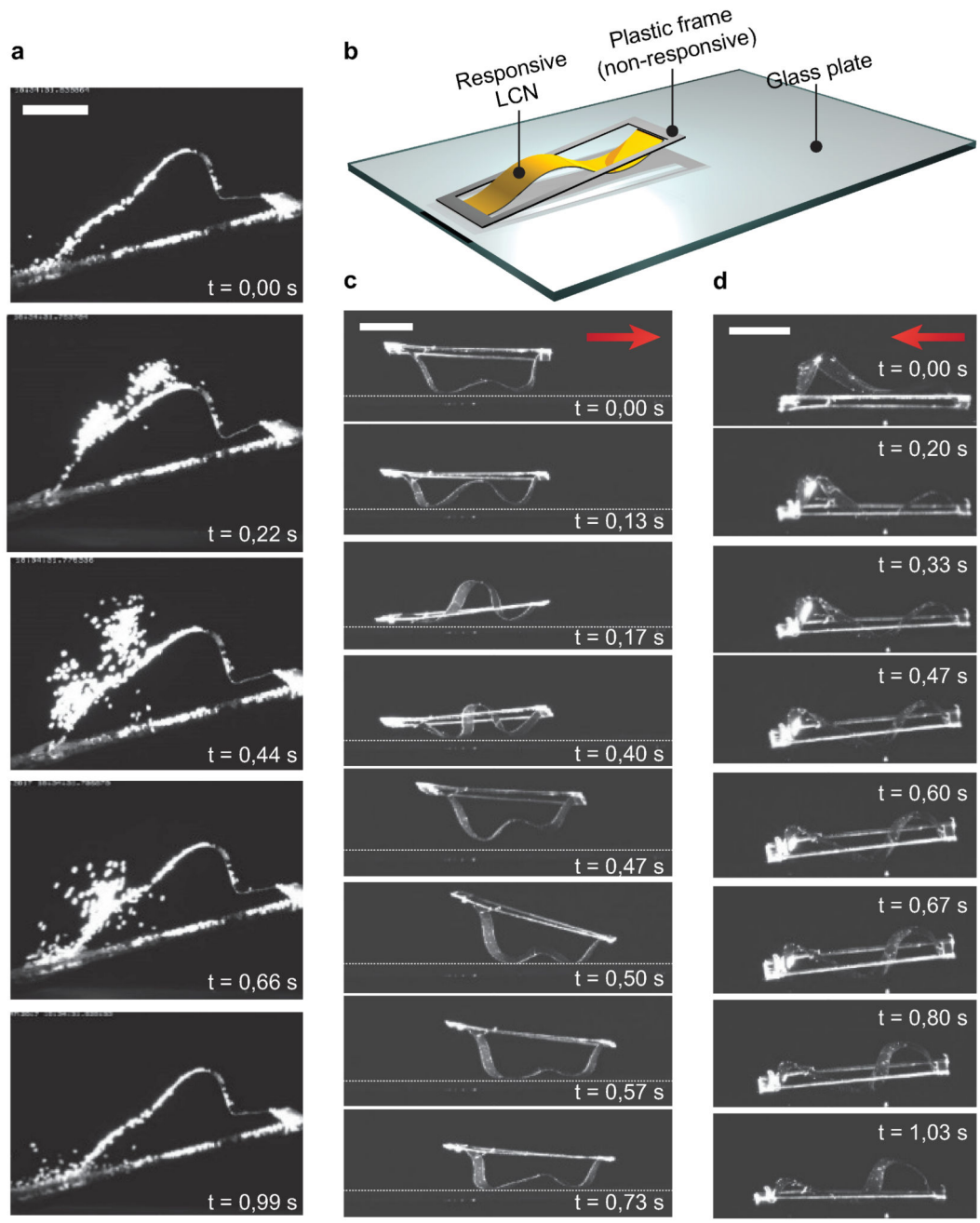

Figure 4. Two examples of applications demonstrating rejection of contaminants and oscillatory transport of a framed film.

a, Photoactuated wave motion ejects sand from the film's surface via a snap-through release of energy, demonstrating the mechanism for a self-cleaning surface. See video S6. **b,** Schematic representation of the photoactuated locomotion along a flat substrate. The short ends of the active film, planar side up (**c**) or homeotropic side up (**d**), are fixed to a passive frame. The direction is dependent on the side exposed. See also video S7 and S8. Active film

composition and dimension: see Figure 2. Plastic frame: 15 mm (length) x 5 mm (width). Scale bar: 5 mm. Dashed line represents the top surface of the glass plates.

Europe PMC Funders Author Manuscripts